Yao *et al. Earth, Planets and Space* (2024) 76:21
https://doi.org/10.1186/s40623-024-01962-4

Earth, Planets and Space

FULL PAPER

Open Access

Current active fault distribution and slip rate along the middle section of the Jiali-Chayu fault from Sentinel-1 InSAR observations (2017–2022)

Jiaming Yao[1,2,3,4], Xin Yao[2,3*], Yanbing Wang[1], Zheng Zhao[4] and Xinghong Liu[2,3]

Abstract

The Jiali-Chayu fault, situated on the eastern side of the eastern Himalayan syntaxis, is the southeastern margin of the large strike-slip fault zone of the Jiali Fault. The study of the distribution and activity within this fault zone is imperative for a comprehensive understanding of the tectonic movement patterns in the southeastern Tibetan Plateau. Previous studies have established that the kinematic characteristic of the Jiali-Chayu fault diverges significantly from that of other segments within the Jiali fault. Nonetheless, the current tectonic characteristics, including the slip sense, slip rate, and geometric deformation of this fault, are still not well resolved, leading to divergent interpretations regarding its contemporary activity intensity. This paper introduced an optimized time-series InSAR method with phase compensation designed for regions characterized by low coherence and exhibiting slow deformation. Using Sentinel-1 SAR data from both ascending and descending orbits spanning the period between 2017 and 2022, we successfully derived deformation rates for the middle part of the Jiali-Chayu fault at a spatial resolution of 150 m. The slip and dip rates of active faults are determined by considering the fault movement rates from two different observation angles, in conjunction with strike angle and the assumed dip angle of the fault. The results show that the deformation rates of the three branches are very different, with F2-1 and F2-2 exhibiting notable activity, while other areas exhibit relatively weaker activity. The strike-slip rates for F2-1 and F2-2 faults range between 3.6 and 5.3 mm/a and 3.05 to 5.13 mm/a, respectively, while their respective dip-slip rates fall within the range of 1.1–2.7 mm/a and 2.99–5.02 mm/a. In accordance with the fault slip directions, we classify the F2-1 fault as a sinistral (left-lateral) strike-slip fault and the F2-2 fault as a dextral (right-lateral) strike-slip fault. This study addresses a gap in remote sensing methods for detecting active fault activity in this region, providing a systematic foundation for identifying weak activity characteristics within the fault zone.

Keywords Jiali-Chayu fault, Time-series InSAR, Strike-slip, Dip-slip, Slip rate

*Correspondence:
Xin Yao
yaoxinphd@163.com
Full list of author information is available at the end of the article

Graphical Abstract

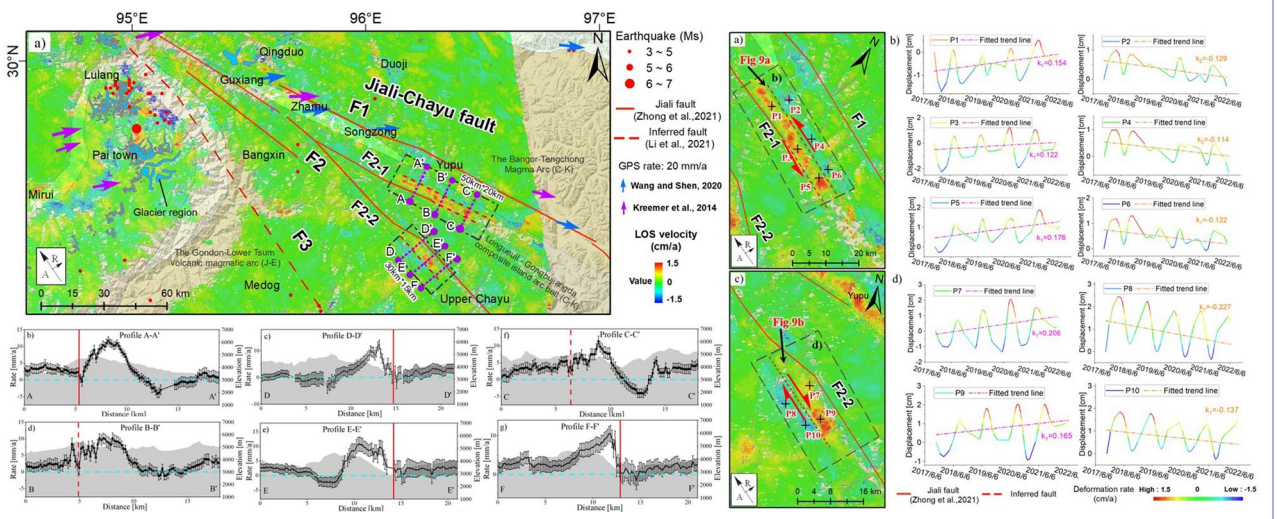

Introduction

The Jiali-Chayu fault is situated at the confluence of the Nyainqentanglha Range and Hengduan mountains, on the eastern side of the eastern Himalayan syntaxis. Additionally, it marks the boundary region of the eastward extrusion of the Tibetan Plateau (Song et al. 2011; Zhang et al. 2021). As one of the major tectonic–geographic boundaries on the eastern margin of the Qinghai-Tibet Plateau, its present-day slip rate has been the focus of research (Collettini et al. 2009). The study of its activity characteristics can directly reflect the origins of regional geological structures and offer a theoretical foundation for elucidating the evolution of the Qinghai-Tibet Plateau (Huang et al. 2021; Ha et al. 2022). Moreover, fault activity plays a crucial role in earthquake prediction along the fault and the assessment of the earthquake cycle (Dalaison et al. 2022; Zhang et al. 2022b). Several fault scarps, trough landforms, and drainage dislocations are evident along the Jiali-Chayu fault zone, indicating strong Late Quaternary activity. Nonetheless, the high and rugged terrain along the fault zone precludes detailed field investigations, resulting in a paucity of research pertaining to the spatial dynamics of the fault zone (Hussain et al. 2016; Scott et al. 2021).

Previous studies suggested that the Jiali fault exhibits strong dextral strike-slip motion, with a slip rate estimated at approximately 10–20 mm/a (Armijo et al. 1989; Wang et al. 2008; Zhao et al. 2015). As the eastern section of the Karakoram-Jiali fault zone, the sense of slip of the Jiali-Chayu fault is significantly different from that of the Jiali Fault (Zhang et al. 2021). In recent years, many scholars have undertaken investigations into the tectonic activity of the Jiali-Chayu fault (Ren et al. 2000; Song et al. 2011; Huang et al. 2021; Li et al. 2021; Zhong et al. 2021). Nonetheless, considerable disparities persist in terms of the fault's nature, spatial distribution, and activity rates. Earlier studies have shown that the Jiali fault zone was not active since the Holocene (Ren et al. 2000; Shen et al. 2003). However, Li et al. (2021) suggests that the activity of the Jiali Fracture has an obvious segmentation. The southeastern section of the Jiali fault exhibits a reversed slip direction, with a strike-slip rate of 3.7–3.8 mm/a and a dip-slip rate of 5.1 mm/a. Song et al. (2011) and Tang et al. (2010), relying on geomorphic indicators like terrace and moraine displacement, have concluded that the Jiali-Chayu fault has transitioned into a left-lateral strike-slip fault in this region, with a slip rate of 3.7 mm/a and a dip-slip rate of 5.1 mm/a (Tang et al. 2010; Song et al. 2011; Liang et al. 2022). In contrast, Zhong et al. (2021) proposed that the Jiali-Chayu fault zone features two branches with slip rates ranging from 1.3 to 2.0 mm/a and dip-slip rates of 2.5–2.9 mm/a. Previous studies on the activity of the Jiali-Chayu fault zone have been carried out through field investigation, geochronology analysis and geomorphological characteristics (Alam et al. 2015). However, due to too sparse measurement points and poor spatial coverage, the activity of the Jiali-Chayu Fracture Zone is highly controversial. The research of the middle section of the Jiali-Chayu fault zone is the most controversial, with the following problems: (1) How many active branch faults are there? Current research predominantly posits the existence of two primary branch faults,

namely the F1 and F2 branch faults, which extend across the area from Zhamu to Guyu and the Upper Chayu region, with their strike direction closely aligned with the southeast. On the southwestern side, a third branch fault (Xixingla fault) is hypothesized based on chronology but lacks definitive confirmation; (2) the present-day activity and movement patterns of these branch faults remain unclear. There is little evidence of current activity on these branching faults, and scholars have differing views on the direction of strike-slip on the faults in the region; 3) the complex geologic environment and weak activities pose a challenge to the observation of deformation rates by traditional geologic methods (Aslan et al. 2019; Özbey et al. 2022). Compounded by the cold, high-altitude setting in which the fault zone is situated, traditional geological survey methods are further impeded.

Significant uncertainties persist in the study of the spatial distribution and activity of the Jiali-Chayu fault, largely owing to the limited availability of geochronological data and GPS information (Friedrich et al. 2003; He et al. 2013). ESA (European Space Agency) has shared long time resolution and wide coverage SAR data from the Sentinel-1 satellite, providing a rare opportunity to measure fault activity (Zhu et al. 2020; Li et al. 2021; Henriquet et al. 2022; Hong et al. 2022; Qu et al. 2022). InSAR methods can obtain deformations with spatial resolution from meters to hundreds of meters (Zhao et al. 2018; Nissen et al. 2022; Yao et al. 2022a; 2022b). By leveraging interferogram pairs with extended temporal spans and precise satellite orbit data, we can systematically monitor tectonic movement and the deformation of active faults (Wicks et al. 2013; Zhao et al. 2022; Wang and Shen. 2020).

In this research, we collected Sentinel-1 ascending and descending SAR data with a time span of 5 years, covering the middle section of the Jiali-Chayu fault zone (Fig. 1). To address the challenge of quantifying fault deformations in regions characterized by weak activity and complex terrain conditions, we introduced a phase-compensation InSAR method aimed at deriving long-term displacement trends. Subsequently, we utilized the optimized InSAR method to compute the strike-slip and dip-slip rates of the fault, enabling us to conduct a comprehensive analysis of the spatial distribution and activity within the middle part of the Jiali-Chayu fault zone.

Tectonic and geological setting

The research area is situated in the southeastern part of the Qinghai-Tibet Plateau and the eastern segment of the Jiali fault. The Jiali fault zone can be divided into three

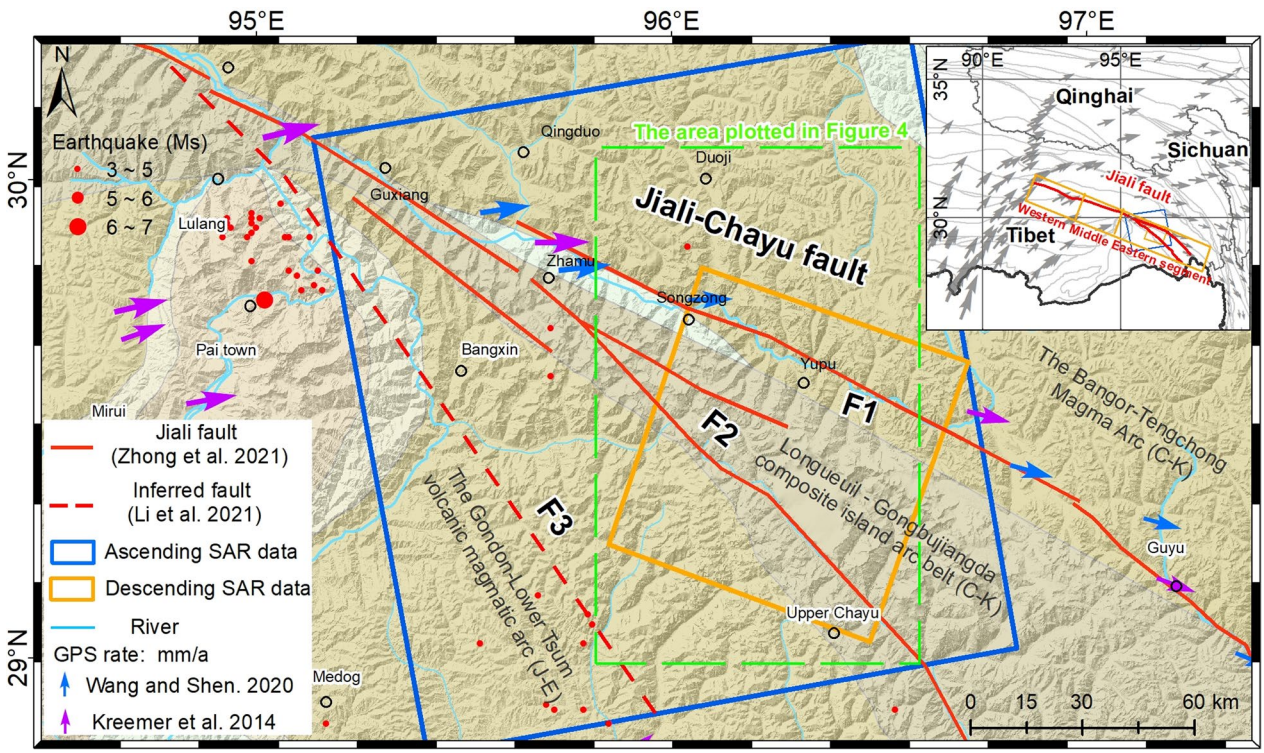

Fig. 1 Topography and faults distribution in the Jiali-Chayu fracture zone (Zhong et al. 2021). GPS rate data were sourced from previous literature (Kreemer et al. 2014; Wang and Shen. 2020), and the segment of the Jiali fault was marked according to Zhang et al. 2021

sections: the northwest-trending Naqu-Jiali fault in the northwestern sector, the northwest-trending Jiali fault in the northern region of the eastern Himalayan syntaxis in the central segment, and the Jiali-Chayu fault in the southeastern area (Armijo et al. 1989; Chen and Khan. 2010; Li et al. 2021). The Jiali-Chayu fault is the eastern section of the Jiali fault zone, which is located at the eastern margin of the Tibetan Plateau and the eastern Himalayan syntaxis in the Yigong-Bomi-Chayu area. This region is classified as part of the Gangdise Himalayan orogenic system, representing a first-order tectonic unit. On a third-level tectonic scale, it can be further subdivided from south to north into the Gondon-Lower Tsum volcanic magmatic arc (J–E), Longueuil-Gongbujiangda composite island arc belt (C–K), and the Bangor-Tengchong Magma Arc (C–K). The elevation of the study area exceeds 5000 m, making it a high-altitude canyon landscape. The natural conditions in this region are challenging, with perennial snow contributing to the presence of numerous glaciers. The geological strata along the Jiali-Chayu fault primarily consist of Jurassic and Cretaceous granites, overlaid with Quaternary glaciers and loose deposits, though preservation of the Quaternary deposits is difficult.

The spatial distribution of the middle part of the Jiali-Chayu fault is shown in Fig. 1. The study area is situated within the central region of the Jiali-Chayu fault zone. Previous studies have suggested that the middle section of the Jiali-Chayu fault zone is located within the Guxiang-Guyu area, and the fault orientation is in the northwest–southeast (NW–SE) direction, extending along the Yigong River and Yarlung Zangbo River (Armijo 1989; Song et al. 2013; Zhong et al. 2021). However, it does not continue to extend into the Hengduan mountains in the southeast (Shen et al. 2003). A substantial mylonite zone has been identified along the fault zone, and it exhibits distinct features such as steep fault segments, troughs, and valley geomorphology, indicative of late Quaternary activity (Armijo et al. 1989). Scholars hold varying perspectives on the branch faults of the Jiali-Chayu fault zone. In Fig. 1, faults F1 and F2, extending along the Yarlung Zangbo River, are regarded as two branch faults of the Jiali-Chayu fault zone (Zhong et al. 2021). The fault strikes for these two branch faults are oriented at approximately 130/140 degrees north by east. On the other hand, Li et al. (2021) and Song et al. (2013) have proposed that the Xixingla fault (F3) represents the southern branch fault of the Jiali-Chayu fault, based on geochronological evidence, although no obvious signs of activity have been observed.

Data and methods

InSAR methodology

To measure long-term fault activity in the study area, we collected Sentinel-1 SAR data (C-band, wavelength 5.6 cm) for total 264 scenes over a 5-year period (Table 1). The Sentinel-1 raw data contain three swaths with nine bursts in each strip. In the initial Single Look Complex (SLC) mosaic process, we merged all 27 subswaths to compute large-scale surface deformation. The SAR images completely covered the study area (Fig. 1). Measuring fault zone activity using the InSAR method presents two primary challenges: (1) in comparison to the deformation rates observed in landslides, land subsidence, and glaciers, the deformation rates associated with active faults are relatively low (Zhang et al. 2019; Li et al. 2020; Wang et al. 2022; Yao et al. 2023). Identifying deformation information with short-baseline interferogram pairs can be particularly challenging; (2) the study area is characterized by rugged mountainous terrain, resulting in diminished coherence within SAR images. Over long-time spans, acquiring continuous displacement data in regions with low coherence presents a challenge, often resulting in data gaps and deformation loss. To address this, we proposed an optimized phase-compensation InSAR method designed to monitor fault zone deformation information. The improvements are as follows: (1) the baseline selection of interferogram pairs was optimized, and interferogram pairs with short vertical baselines and long baselines were screened to reduce incoherence and increase the deformation signal; (2) we introduced a phase compensation method through the utilization of the Stacking method. This approach uses interferogram pairs with good coherence to initially estimate the linear deformation rate and subsequently perform spatial interpolation. The deformation rate, multiplied by the time interval of the interferogram pairs, is applied to areas masked by low coherence or missing data in other interferograms. The temporal deformation within the fracture zone region was extracted through

Table 1 Sentinel-1 SAR images and parameters

Data	Pixel spacing	Time	Path and frame	No. of images	Total interferograms	Interferograms used
Sentinel-1 ascending	Range 2.3 m, azimuth 14 m	10/18/2017–06/18/2022	70–1277	133	2091	28
Sentinel-1 descending	Range 2.3 m, azimuth 14 m	10/08/2017–05/15/2022	106–496	131	1950	34

the singular value decomposition (SVD) processor of SBAS method.

The data processing workflow is as follows: (1) initially, all SAR images were co-registered using precise orbit files, achieving a co-registration accuracy of approximately 0.1 pixels. To save computing time and improve computing efficiency, SAR images were cropped to focus on the study area. (2) Temporal and spatial baselines were set at 1500 days and 20 m (Fig. 2a). Multi-looks parameter was set to 50:10 in range and azimuth directions, and the interferogram pairs were initially filtered by an adaptive filter with a window size of 128 pixels and a step size of 4 pixels. (3) A coherence threshold of 0.3 was applied, and the Minimum Cost Flow (MCF) method was employed to unwrap the interference phase (Lyons and Sandwell. 2003). In regions characterized by snow and ice, where the ground's reflectivity to radar signals is poor, and these areas were masked during the phase unwrapping process. In the error removal process, the perpendicular baselines were utilized to infer and subsequently correct DEM errors (Fattahi and Amelung. 2013; Zhang et al. 2022a). It is worth noting that there exists a correlation between terrain elevation and atmospheric error (Devaraj and Yarrakula. 2020). In this paper, we developed a height/atmosphere correlation fitting model to mitigate atmospheric errors from the unwrapped interference phase. While ionospheric errors are known to be present in high and mid-latitude regions (Bowman and Dunne. 1981; Zhang et al. 2022c; Mao et al. 2023), no obvious ionospheric errors were observed in the interferogram pairs.

The process of the optimized phase compensation method is shown in Fig. 2b: (1) high coherence points were selected, and their phase information was extracted from high-quality long-term baseline interferogram pairs. The initial linear deformation rate was estimated using the Stacking method (Lyons and Sandwell. 2003). Compared with the Average-DInSAR method (Yao et al. 2021), the stacking method avoids the underestimation of the deformation rate due to the introduction of null values; (2) kriging interpolation (Yao et al. 2020) was employed to model the phase of low-coherence regions based on the initial deformation rate. It is important to mention that the low-coherence regions exclude shadow and overlay areas, which were appropriately masked; (3) the simulated phase was then used to compensate for the low-coherence regions in other interferogram pairs, effectively replacing the displacement information within low coherence or missing data regions of lower-quality interferometric pairs; (4) using the singular value decomposition (SVD) method within SBAS technique, an improved average deformation rate and time-series deformation were derived. Figure 3 provides a visual representation of the temporal displacement estimation at the deformation point. Phase losses were substituted in the time domain by the initial stacking linear deformation rate (black triangles). Subsequently, the stacking method was reapplied for calculating the linear deformation rate. After several iterations, ultimately the simulated time-series deformation of the deformation point was obtained.

GNSS data and previous results

We collected velocity data from GPS stations within the eastern Tibetan Plateau, as documented by Kreemer et al. 2014 and Wang and Shen. 2020. Thirteen reliable

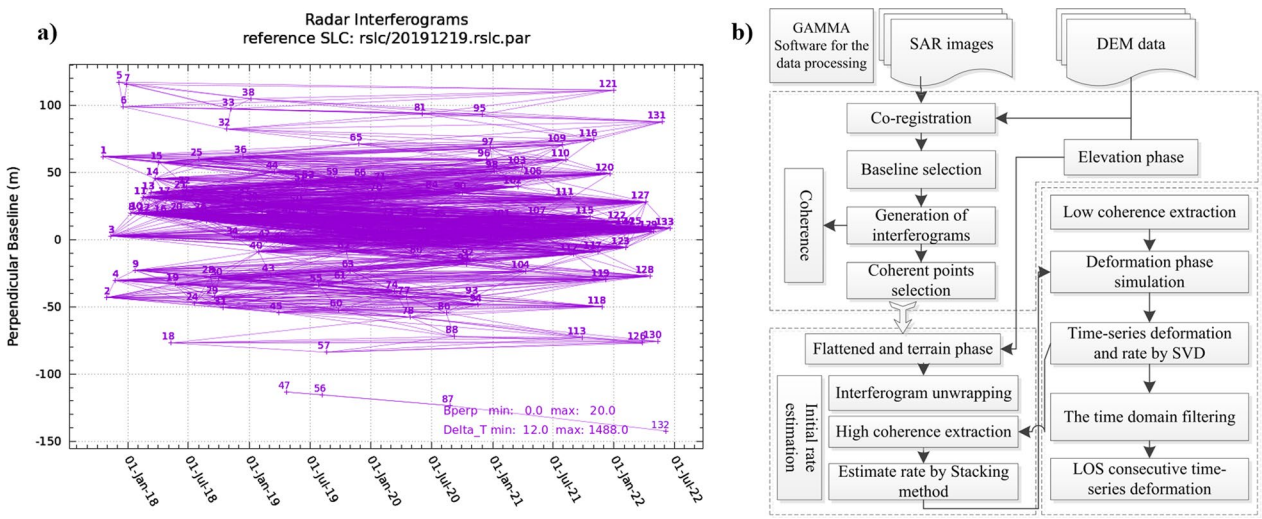

Fig. 2 The spatiotemporal baselines of ascending orbit and workflow of the InSAR method

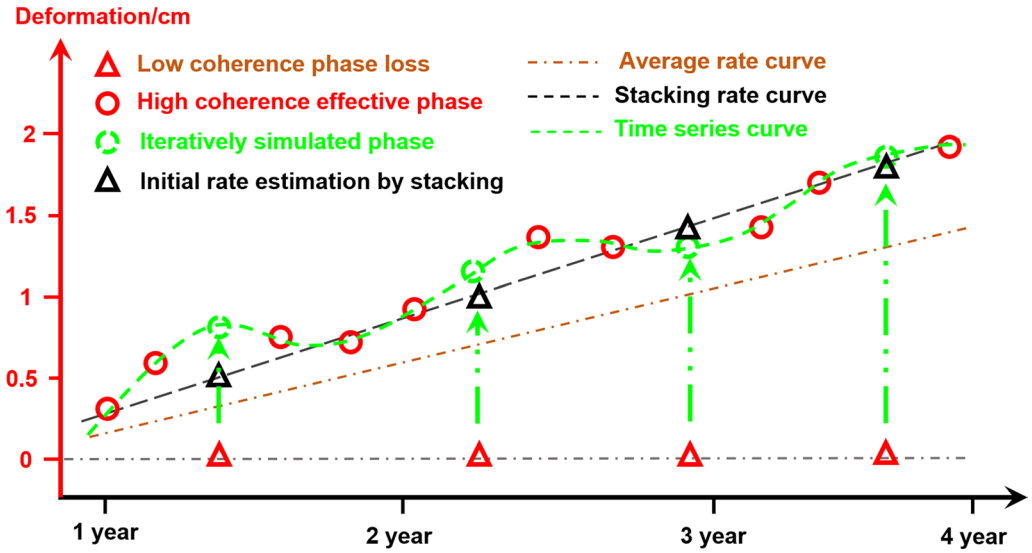

Fig. 3 Schematic diagram of phase compensation method. Highly coherent phases were represented by red circles, iteratively simulated phases by green circles, and phase losses due to low coherence by red triangles

data points within the study area were extracted and are detailed in Table 2. It is essential to note that the GPS data from various sources are all anchored in a Eurasia-fixed reference frame. Furthermore, data recorded in the relevant literature are presented in Table 3. While the available GPS monitoring points may be relatively sparse, they serve as valuable reference points for comparative analysis alongside the InSAR measurements. This comparative approach allows us to assess fault zone activity characteristics in the study area, guided by geological findings from previous literature. The spatial interpolation of GPS station data was carried out using the Kriging interpolation method. The phase-unwrapped point in the InSAR method was used as reference point for correcting the GPS interpolation rates. These GPS interpolation rates provide insights into the regional surface activity rate. Additionally, east–west and north–south regional rates were derived through vector velocity decomposition. The interpolation rate was compared with InSAR results, and the difference between fault activity and surrounding area was analyzed.

Results

Regional deformation

In contrast to the conventional small baseline subset (SBAS) method, our approach, which focuses on

Table 2 GPS data used in the study

Num	Station	Longitude	Latitude	Ve (mm/a)	Vn (mm/a)	Resource
1	J011_GPS	95.601	29.939	19.5	2.9	Wang and Shen. 2020
2	J319_GPS	95.79	29.819	20.1	2.4	Wang and Shen. 2020
3	J389_GPS	96.095	29.75	17.3	0.5	Wang and Shen. 2020
4	J393_GPS	96.885	30.055	18	− 1.9	Wang and Shen. 2020
5	J395_GPS	97.181	29.282	14.5	− 4	Wang and Shen. 2020
6	JB50_GPS	96.868	29.391	16.5	− 4.6	Wang and Shen. 2020
7	BAYI_GPS	94.728	29.684	17.0	6.0	Kreemer et al. 2014
8	GYX1_GPS	97.217	29.153	15.0	− 5.3	Kreemer et al. 2014
9	LLZ1_GPS	94.724	29.737	20.8	4.9	Kreemer et al. 2014
10	PQX1_GPS	94.892	29.541	19.1	3.4	Kreemer et al. 2014
11	RWZ1_GPS	96.763	29.505	16.8	− 4.2	Kreemer et al. 2014
12	TOM1_GPS	95.085	30.103	21.6	5.4	Kreemer et al. 2014
13	ZMZ1_GPS	95.738	29.87	21.2	0.4	Kreemer et al. 2014

Table 3 Literature data in the study

Num	Slip rate (mm/a)	Dip-slip rate (mm/a)	Location	Resource
1	10 ~ 20	–	Jiali county	Armijo et al. 1989
2	4.0	–	Jiali-Chayu	Ren et al. 2000
3	2.0 ~ 3.0	–	Tongmai-Xiachayu	Shen et al. 2003
4	3.7 ~ 3.8	5.1	Tongmai-Chayu	Song et al. 2011
5	3.7 ~ 4.0	–	Tongmai-Xiachayu	Song et al. 2013
6	3.0 ~ 5.0	–	Tongmai-Xiachayu	Tang et al. 2010
7	1.3 ~ 2.0	2.5 ~ 2.9	Songzong town	Zhong et al. 2021
8	3.7 ~ 3.8	5.1	Tongmai-Xiachayu	Li et al. 2021

selecting interferogram pairs with short perpendicular and long temporal baselines, significantly reduces the occurrence of low-coherence regions while facilitating the generation of a complete deformation field. Figure 4 shows four selected high-quality interferogram pairs obtained by applying this method. In the interferogram results with long-time span, the Jiali-Chayu fracture zone exhibits deformation. Figure 5 compares the results obtained through the traditional SBAS method and proposed approach in this paper. It can be seen that there are many blank areas in the SBAS results, which are due to the phase loss of some time periods caused by incoherence, resulting in the loss of time-series results. After phase compensation, the optimization method can estimate the time-series deformation of the entire region better.

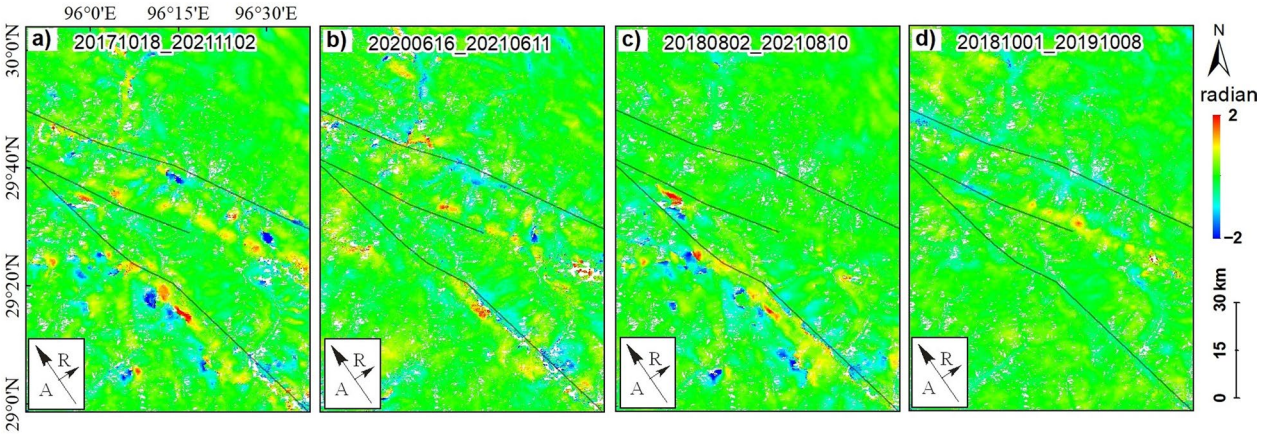

Fig. 4 Examples of selected high-quality interferogram pairs from ascending track 70–1277. The black line shows the Jiali-Chayu fault zone. The deformation data within the white region are absent, which is a low coherent reflection area caused by snow and ice. A and R represent azimuth and range observation directions of the satellite

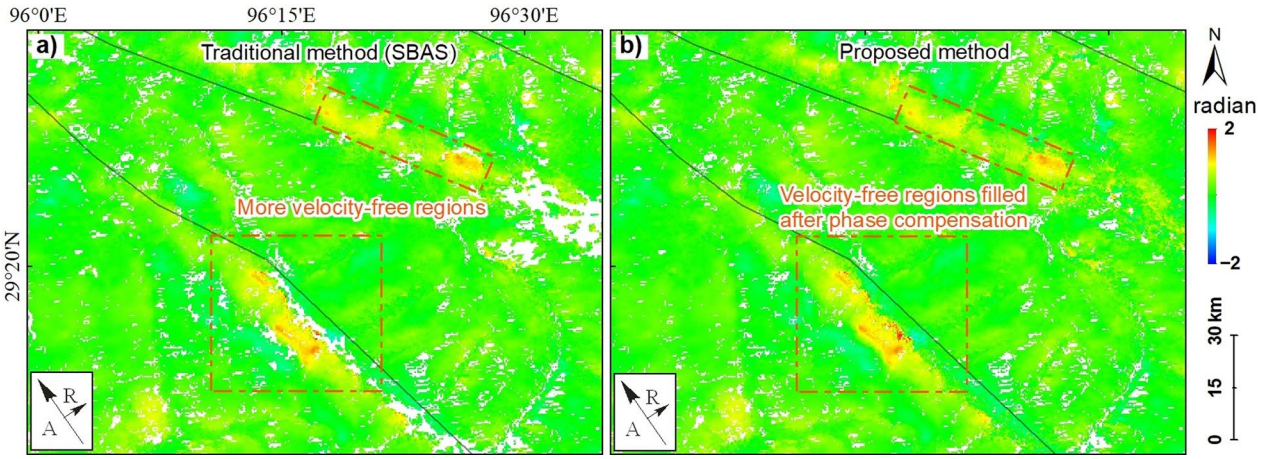

Fig. 5 Comparison between the proposed method and the traditional method (SBAS)

We integrated Stacking and SBAS techniques, as detailed in Sect. "InSAR methodology", to further derive the long-term average velocity field of the fault zone. Figure 6 presents the average line of sight (LOS) velocity field within the fault zone region during the period 2017–2022, acquired from ascending SAR images. Additionally, the figure includes six velocity profiles spanning the fault zone, with a focus on F2-1 and F2-2. Notably, the activity of the three branch faults inferred within the middle section of the Jiali-Chayu fault zone is different. The F2 fault, situated in the central region, exhibits activity, marked by differential displacement along the southeastern margin of the fault zone. The maximum LOS deformation value in this area reaches approximately ± 15 mm/a.

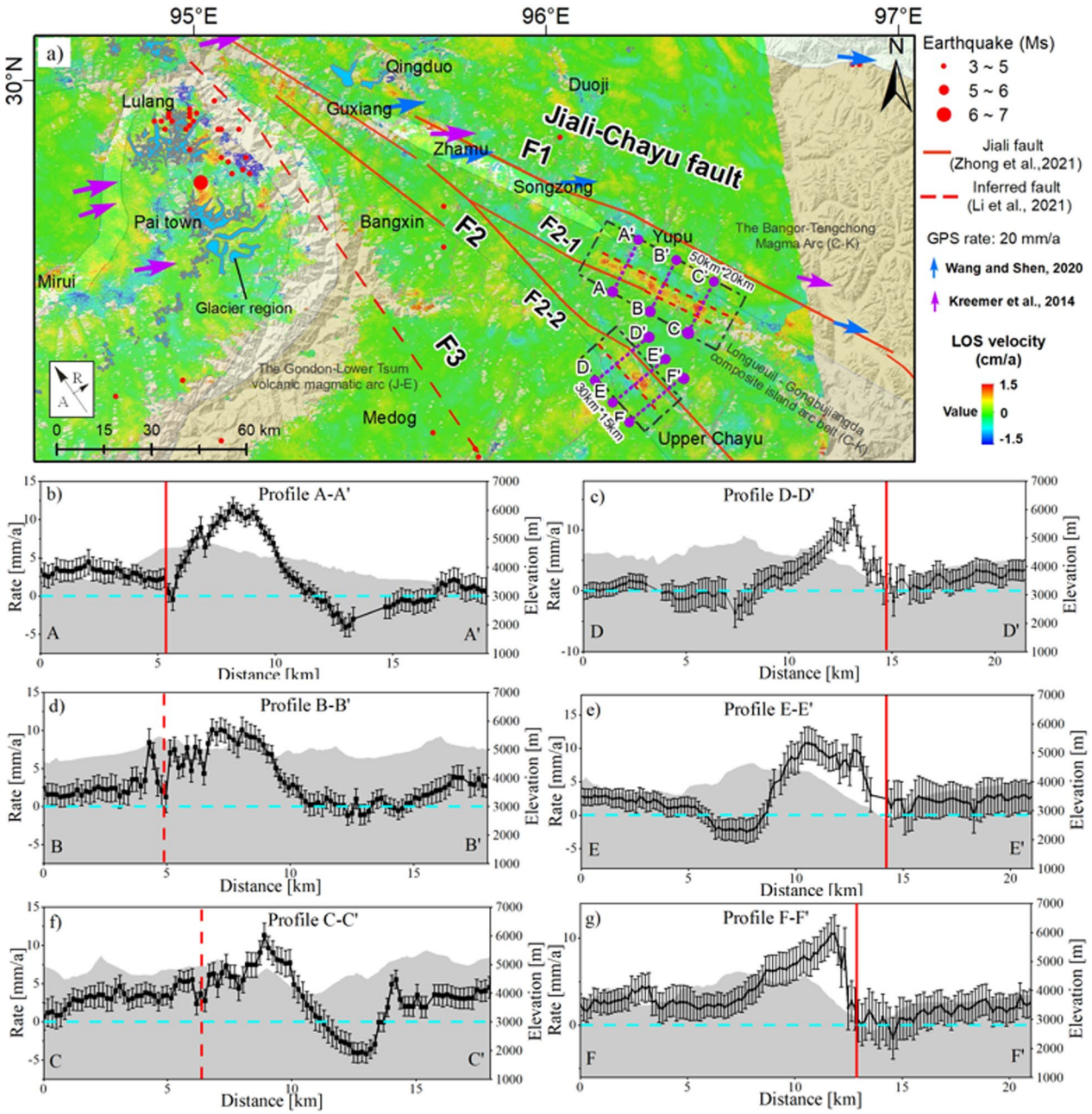

Fig. 6 Line-of-sight (LOS) velocity and six profiles along the fault acquired from Sentinel-1 ascending SAR images. Negative (blue) and positive (red) values indicate relative ground motion toward and away from the SAR satellite, respectively. **a** Average LOS velocity; **b**, **d**, **f** three velocity profiles of Fault F2-1 along purple lines (AA', BB', and CC') as marked in **a, c**, **e**, **g**. Three velocity profiles of Fault F2-2 along purple lines (DD', EE', and FF') as marked in **a**. The glacier boundaries are sourced from the Second Chinese Glacier Inventory dataset (http://www.ncdc.ac.cn

Conversely, the F1 and F3 faults, located in the north and south (Li et al. 2021), display limited activity.

Six velocity profiles were generated across the two F2 fault zones, namely F2-1 and F2-2, for an in-depth analysis of displacements within the active zone of the fault area (Fig. 6b–g). The active zone is located in the black box in Fig. 5a, and the rectangular active extent of the fault is determined based on observed displacement patterns on either side of the fault. F2-1 encompasses an active fault zone spanning approximately 50 km in length and 20 km in width. As shown in Fig. 6b, d, f, three velocity profiles were plotted for the active zone of the F2-1 fault. Within the region traversed by the 5 km fault, noticeable deformation is evident, with the area located 10 km northeast of the fault exhibiting opposite motion characteristics. The eastern side of the fracture zone displaces towards the southeast relative to the western side. The maximum LOS deformation rate on the east and west sides is approximately 5 mm/a and 15 mm/a, respectively. The active characteristics of the F2-1 fault diminish southeast of profile C–C′. Figure 5c, e, g provides velocity profiles of F2-2 branch fault, situated to the south of F2. This fault extends from Yigong to the Lower Chayu area. The fault strike determined through remote sensing techniques aligns closely with that recorded in the existing literature, with a recorded fault strike of 140 degrees north by east. The active fault zone of F2-2 spans around 30 km in length and 15 km in width, with an activity rate of approximately 10 mm/a. The profiles reveal differential deformation on the west side of the fault zone.

Based on the optimized phase compensation method (Sect. "InSAR methodology"), we computed time-series deformation for two active faults. Figure 7 displays the time-series deformation of the F2-1 and F2-2 faults. Figure 7a, b presents the deformation rate of the F2-1 fault zone and the time-series displacement on both sides of the fault zone. We consider that the temporal deformation contains three components: seasonal displacement variations, tectonic displacement, and other errors. The seasonal displacement variations caused by strong seasonal temperature variations are all manifested as temperature-dependent wave-like displacement changes during freeze–thaw cycles. Tectonic displacement can be revealed by trend line fitting methods. Other errors may be localized systematic errors. Subsequent tectonic displacement rates were subjected to linear fitting to mitigate the impact of non-tectonic influences. We selected stable scattering points on either side of the fault, situated on exposed bedrock, in order to mitigate errors caused by snow and ice. Time-series displacement for three points (P1, P3, and P5) reveals an annual line-of-sight (LOS) rate of 3–5 mm/a in the western segment of the inferred F2-1 fault (marked by the red dashed line in Fig. 6a), while points (P2, P4, and P6) indicate an average annual LOS rate of 3–3.5 mm/a.

We also utilized Sentinel-1 descending images to assess surface deformation in the region, which helped evaluate the reliability of displacement in the fault area. Figure 8 presents the spatiotemporal baselines and the surface deformation field derived from descending SAR images. It is evident that deformation patterns similar to those in Fig. 6a are observed near the F2-1 and F2-2 faults. The spatial locations of the localized deformation regions align with the results from the ascending images, extending along the direction of the fault line. Variations in the observed line of sight (LOS) deformation values are attributed to the disparities in satellite observation angles. Nevertheless, leveraging the multi-angle observations enables us to calculate the fault components, including strike-slip and dip-slip rate components, facilitating the analysis of the fault slip velocity.

Fault slip rate and motion pattern

Figure 9 shows the Quaternary active faults detected in the middle part of the Jiali-Chayu fault zone, along the ridge line direction, based on the deformation field. The linear structural pattern of the active fault area is evident, and the areas of fault compression predominantly consist of bedrock fracture zones or formed troughs (Fig. 9a). The F2-1 fault zone exhibits near north–south strike-slip movement, generating shear stress that disrupts the nearby rock mass structures, contributing to glacier formation. The significant development of debris flows in the fracture zone crossing area suggests ongoing fault activity. Figure 9b displays the fault escarpment and fault facet formation in the F2-2 fault zone, with the canyon region undergoing subsidence. However, the high altitude of the area poses challenges in exploring geological evidence of the fracture zone. Based on the spatial distribution of the deformation area, we determined the precise location of the active fault in the middle part of the Jiali-Chayu fault zone. The fault strike observed in this study using InSAR is basically consistent with previous literature findings, with both branch faults exhibiting a nearly southeast direction (Zhong et al. 2021). Utilizing the observation principles of the Sentinel-1 SAR satellite and considering the characteristics of fault motion, we performed an analysis to determine the sense of slip for the active F2-1 and F2-2 faults.

The fault zone movement can be decomposed into strike-slip and dip-slip components. In this paper, surface displacement decomposition equations were established by utilizing the known fault strike as a constraint condition and assuming the dip angle of 70 degrees for the faults. Following the principles of radar observation, the radar line-of-sight (LOS) deformation value results from

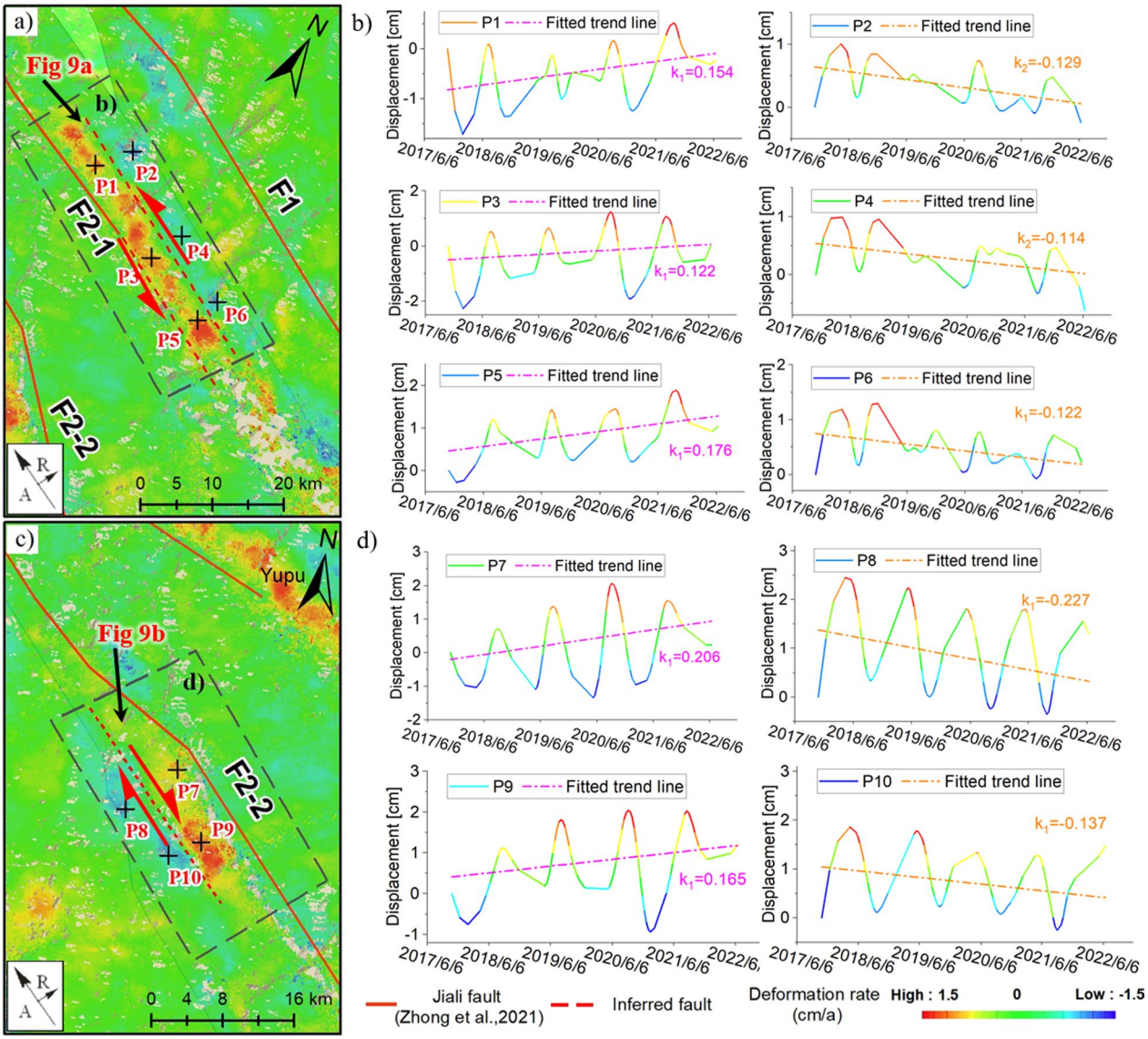

Fig. 7 Time-series movement of two branch fault zones within the Jiali-Chayu fault zone. The red dashed line in **a** indicates the location of the detected fault zone. Negative (blue) and positive (red) values indicate relative ground motion toward and away from the SAR satellite, respectively. "k" represents the average fitted rate (cm/a), and the color of trend lines indicate deviations from the trend of the average LOS change rate. The dashed rectangles in **a** and **c** represent the fault locations in Fig. 9

contributions of both the fault's strike-slip ($\boldsymbol{d_s}$) and dip-slip ($\boldsymbol{d_d}$) components. LOS deformation (d^A_{los}, d^D_{los}) obtained by ascending and descending SAR images can be decomposed into d_d and d_s components (formulas 1 and 2), allowing for the resolution of the two unknowns through a pair of independent equations (Yao et al. 2022a; Liu et al. 2022).

$$\begin{aligned} d^A_{los} = &- d_d \cdot \cos\left(\theta^A_{inc} - (\pi/2 - \theta_d)\right) \\ &\cdot \sin\left(\theta^A_{azi} - \theta_f + \pi/2\right) \\ &- d_s \cdot sin\theta^A_{inc} \cdot \cos\left(\theta^A_{azi} - \theta_f + \pi/2\right), \end{aligned} \tag{1}$$

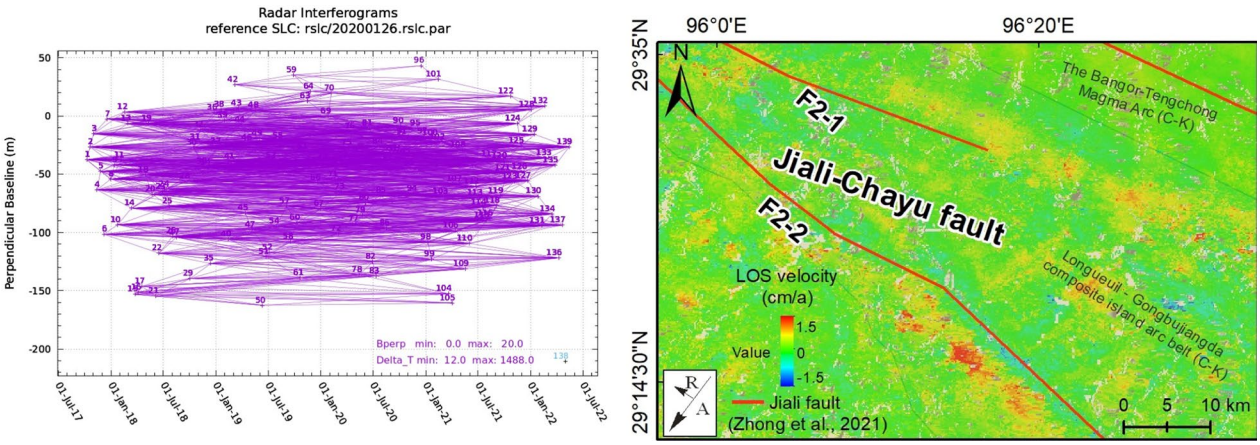

Fig. 8 The spatiotemporal baselines and surface deformation derived from Sentinel-1 descending images

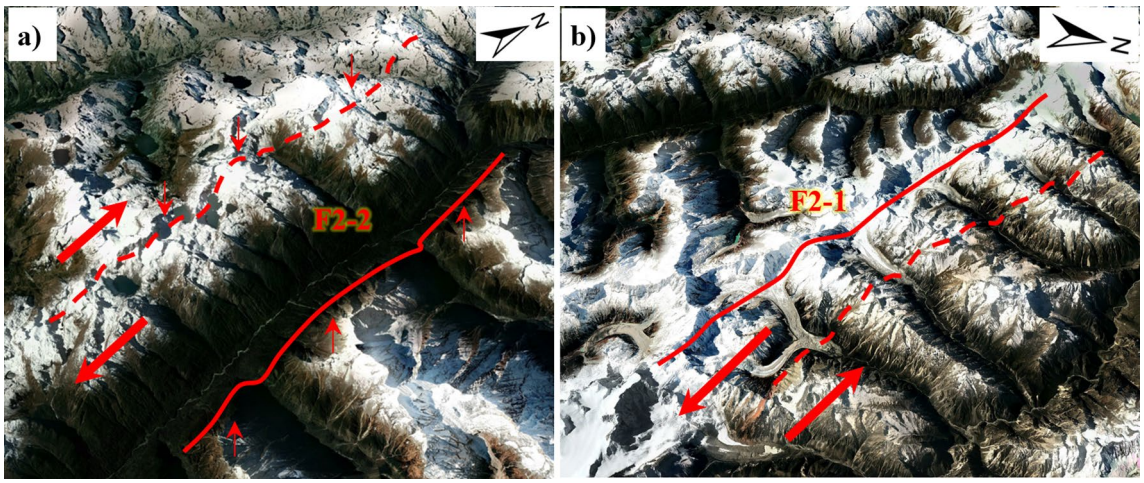

Fig. 9 Two branch faults of the Jiali-Chayu fault as observed in Google Earth images. **Figure 7**a and c provides the locations of the two active fault zones. Solid red lines are already-known fault trace and dashed red lines are inferred faults

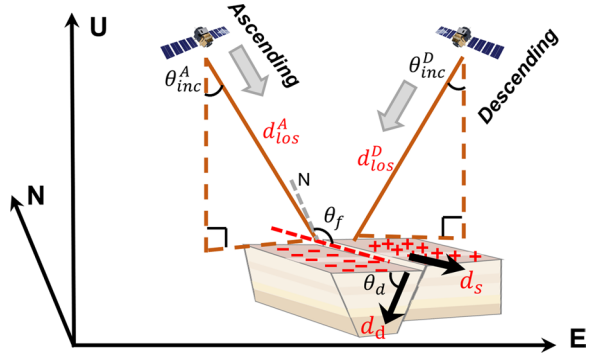

Fig. 10 Schematic diagram of fault movement velocity decomposition. "+" and "−" in the figure indicate ground uplift and subsidence, respectively

$$
\begin{aligned}
d^D_{los} = &- d_d \cdot \cos\left(\theta^D_{inc} - (\pi/2 - \theta_d)\right) \cdot \\
&\sin\left(\theta^D_{azi} - \theta_f + \pi/2\right) \\
&- d_s \cdot sin\theta^D_{inc} \\
&\cdot \cos\left(\theta^D_{azi} - \theta_f + \pi/2\right).
\end{aligned} \tag{2}
$$

Figure 10 shows the motion vector decomposition diagram, where θ_{inc}, θ_{azi} θ_d and θ_f represent the incidence angle, azimuth angle, dip and strike angles of the fault, respectively. Detailed parameters are shown in Table 4. By employing motion vector decomposition, we derived the motion rates of active faults. These motion rates for F2-1 and F2-2 faults are documented in Table 5. In Fig. 10, the

Table 4 Satellite observations and fault motion angles (degrees)

θ_{inc}^{A}	θ_{inc}^{D}	θ_{azi}^{A}	θ_{azi}^{D}	θ_f	θ_d
39.6	43.9	− 12	192.7	130 (F2-1) 140 (F2-2)	70

Table 5 Strike-slip, and dip-slip deformation rates of F2-1 and F2-2 faults

Fault	d_s(mm/a)	d_d(mm/a)	Nature
F2-1 East	− 1.80 ~ − 2.16	0.55 ~ 1.05	Left-lateral strike-slip normal fault
F2-1 West	1.85 ~ 3.1	− 0.55 ~ -1.65	
F2-2 East	− 1.85 ~ − 2.78	− 1.45 ~ -2.64	Right-lateral strike-slip normal fault
F2-2 West	1.2 ~ 2.35	1.54 ~ 2.38	
F2-1 relative rate	3.65 ~ 5.26	1.10 ~ 2.70	–
F2-2 relative rate	3.05 ~ 5.13	2.99 ~ 5.02	–

direction of movement is indicated by positive and negative values of the activity rate.

In the calculation process, negative values were assigned to the strike-slip component (d_s) along the fault in the near SE direction and the dip-slip component (d_d) along the downward direction. The results indicate that the relative strike-slip rate on both sides of the F2-1 fault ranges from 3.65 to 5.26 mm/a, and the dip-slip rate is approximately 1.1–2.7 mm/a. The relative movement between the two fault plates helps determine the fault type. Based on the relative uplift and eastward movement observed on the east side of the fault, we infer that the F2-1 fault is a left-lateral strike-slip normal fault. Similarly, the relative strike-slip rate on both sides of the F2-2 fault is approximately 3.05–5.13 mm/a, and the dip-slip movement rate is about 2.99–5.02 mm/a. The subsidence and eastward movement characteristics on the east side of the fault indicate that the F2-2 active fault is a right-lateral strike-slip normal fault.

The activity within the middle section of the Jiali-Chayu fault zone exhibits segmentation. F2-1 and F2-2 active faults stand out as the most active areas in this part of the Jiali-Chayu fault zone, situated in the fault's extension zone. Based on the calculated motion rates of these two active faults, a movement model for these active faults has been formulated (Fig. 11). The model provides a visual representation of the fault movement, with red arrows in the figure denoting the direction of movement for the two fault plates.

We performed GPS data interpolation from the Qinghai-Tibet Plateau region (Wang and Shen. 2020) and conducted a comparison of fault zone activity rates with historical literature and interpolated GPS data (Fig. 12). GPS data interpolation was carried out using the Kriging method, with the reference point selected for InSAR deformation calculations serving as the reference for relative GPS velocity field calculations. In Fig. 12b, c, the dashed red area delineates the fault activity rates calculated in this study and speculated upon in previous literature. Our findings reveal that the F2-1 and F2-2 active faults within the middle part of the Jiali-Chayu fault zone exhibit relatively higher activity levels in the eastern region of the eastern Himalayan syntaxis, with activity rates slightly surpassing those of the spatial GPS interpolation. The magnitudes of deformation are consistent. Furthermore, the slip rates in the active areas of the fault zone (F2-1 and F2-2 fault

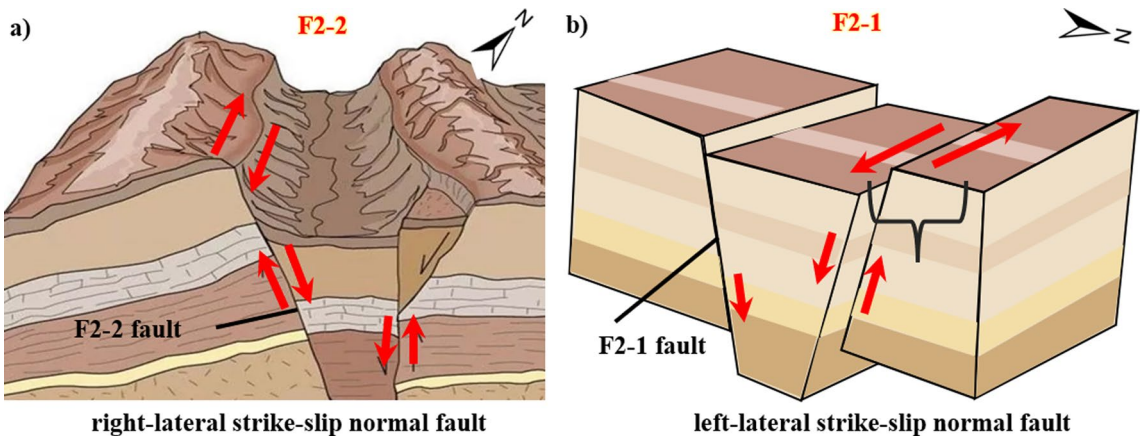

Fig. 11 Schematic diagram of two active faults motion model. **a** Modified according to the geological model diagram of V-type fault: https://www.facebook.com/engineeringinfinity.co/posts/a-spectacular-v-shaped-fault-at-zanjan-on-the-road-between-tabriz-and-tehran-in-/926316871506483. **b** Schematic of F2-1 strike-slip faults

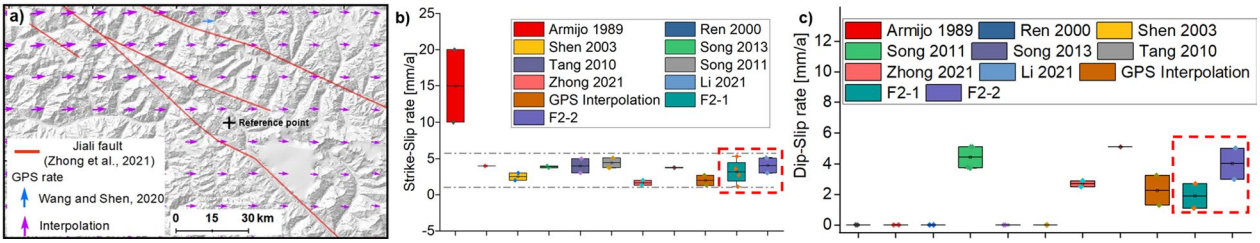

Fig. 12 Previous studies on the strike-slip and dip-slip rates of the Jiali-Chayu fault. **a** GPS velocity field and InSAR reference point position The data in the red box area in **b** and **c** are the strike-slip and dip-slip rates calculated in this paper

zones) calculated in this study are slightly greater than the strike-slip rates estimated in previous literature. However, it's important to note that other branches of the Jiali-Chayu fault zone display very weak activity, with rates in the range of 0–2 mm/a.

Discussion

Given the weak fault activity, the conventional InSAR method struggles to accurately capture fault activity. In this paper, we introduced the optimized phase-compensated InSAR method to obtain a high-resolution deformation field at 150 m resolution, and the time-series deformation field results reveal freeze–thaw cycle deformation characteristics (Fig. 7). Our results indicate that fault activity in the middle section of the Jiali-Chayu fault zone exhibits spatial heterogeneity. When compared with previous literature and GPS rate interpolation results, the activity rates of the actively faulted zones, F2-1 and F2-2, monitored in this study are marginally higher. Moreover, activity levels in other regions are low, and the overall movement in the fracture zones is not extensive. Previous studies estimated the activity rate of the Jiali-Chayu Fracture Zone primarily based on discrete geological evidence and sparse GPS monitoring sites, leading to discrepancies in the estimation of this zone's activity rate. Furthermore, the activity pattern of the middle section of the Jiali-Chayu Fracture Zone inferred from previous studies remains contentious. Specifically, the F2-1 and F2-2 fracture zones are identified as left-lateral strike-slip normal fault and right-lateral strike-slip normal fault, respectively, implying that the tectonic movement in the study area is complex, and a singular tectonic movement pattern does not apply.

While there are numerous active faults on the Tibetan Plateau, their current activities remain largely unknown. Monitoring fault activity comprehensively on a large scale using discrete GPS monitoring data is challenging. Conversely, the InSAR method proposed in this paper offers effective identification capabilities for fault activity studies, enabling the identification of active fault zones on a broad scale over an extended timeframe. The findings presented in this paper provide valuable data to better understand the activity characteristics of the Jiali fault and the significance of the East Himalayan tectonic synergy zone's motion.

Conclusions

In this study, we introduce an optimized phase compensation method to derive the deformation rate of the fracture zone. We process Sentinel-1 ascending and descending SAR data with a period of 5 years to generate the surface deformation field within the middle of the Jiali-Chayu fault zone. Leveraging the available fault distribution information and deformation field data, we perform an analysis of the spatial distribution and slip rates of active faults in the central region of the Jiali-Chayu fault zone. This research addresses the gap in remote sensing-based fault activity detection in the region and offers valuable insights for understanding fault zone activity, disaster development, and engineering construction. The key findings are as follows:

(1) The deformation within the fracture zone is of very low magnitude, often at the millimeter per year scale, making it a challenge for conventional InSAR methods to effectively capture. The optimized InSAR method introduced in this study offers improved detection capabilities for identifying weak, large-scale deformations resulting from fault movements. Through the extraction of phase information from both long-time and short-baseline interferogram pairs, we can effectively obtain time-series deformation data within the fracture zone, accurate to the millimeter level.

(2) Long time-series InSAR measurement results show differences in the activity of three branch faults (F1, F2, F3) in the middle part of the Jiali-Chayu fault zone. While the F1 and F3 fractures exhibit weak activity, characterized by deformation rates in the range of 0–2 mm/a, the F2 branches (F2-1 and F2-2) display strong activity.

(3) Based on the InSAR measurement results, we conducted an in-depth analysis of fault activity and slip rates. The F2-1 fault is identified as a left-lateral strike-slip normal fault with a strike-slip rate ranging from 3.6 to 5.3 mm/a, and a dip-slip rate from 1.1 to 2.7 mm/a. Conversely, the F2-2 fault is categorized as a right-lateral strike-slip normal fault, with a strike-slip rate varying from 3.05 to 5.13 mm/a and a dip-slip rate within the range of 2.99–5.02 mm/a.

(4) The slip rates of the Jiali-Chayu fault have been a subject of contention in prior research. The observed activity within the fault zone suggests that the Jiali-Chayu Fault Zone is not characterized by a singular left-lateral or right-lateral strike-slip motion. Instead, it consists of fault zones with varying degrees of activity and tectonic motion. The activity rates of the two active faults detected in this study are comparatively higher when contrasted with the estimated activity rates of the fault zones based on prior research and GPS interpolation. Conversely, the activity rates in other regions are relatively weaker.

Acknowledgements
We are very grateful for the Sentinel-1A data provided by European Space Agency (ESA).

Author contributions
JY conceived the manuscript; XY and YW provided funding support and helped improve the manuscript; ZZ and XL provided relevant data.

Funding
This work was supported by the Science and Technology Project of State Grid Corporation of China (No. 5200-202356393A-2-4-KJ), the Chinese Geological Survey Project (No. DD20230433).

Availability of data and materials
Sentinel-1A data used in this study were provided by the European. Space Agency (ESA) through the Sentinel-1 Scientific Data Hub.

Declarations

Competing interests
The authors declare no competing interests.

Author details
[1]State Grid Economic and Technological Research Institute Co., Ltd, Beijing 102209, China. [2]Institute of Geomechanics, Chinese Academy of Geological Sciences, Beijing 100081, China. [3]Key Laboratory of Active Tectonics and Geological Safety, Ministry of Natural Resources, Beijing 100081, China. [4]University of Chinese Academy of Sciences, Beijing 100049, China.

Received: 18 August 2023 Accepted: 6 January 2024
Published online: 30 January 2024

References

Alam A, Ahmad S, Bhat M, Ahmad B (2015) Tectonic evolution of Kashmir basin in northwest Himalayas. Geomorphology 239:114–126. https://doi.org/10.1016/j.geomorph.2015.03.025

Armijo R, Tapponnier P, Tonglin H (1989) Late Cenozoic right-lateral strike-slip faulting in southern Tibet. J Geophys Research-Solid Earth Planets 94(B3):2787–2838. https://doi.org/10.1029/JB094iB03p02787

Aslan G, Lasserre C, Cakir Z, Ergintav S, Özarpaci S, Dogan U, Bilham R, Renard F (2019) Shallow creep along the 1999 Izmit Earthquake rupture (Turkey) from GPS and high temporal resolution interferometric synthetic aperture radar data (2011–2017). J Geophys Research-Solid Earth 124(2):2218–2236. https://doi.org/10.1029/2018JB017022

Bowman GG, Dunne GS (1981) Some initial results on mid-latitude spread-f irregularities using a directional ionosonde. J Atmos Terr Phys 43(12):1295–1307. https://doi.org/10.1016/0021-9169(81)90155-0

Chen LZ, Khan SD (2010) InSAR observation of the strike-slip faults in the northwest Himalayan frontal thrust system. Geosphere 6(5):731–736. https://doi.org/10.1130/GES00518.1

Collettini C, Niemeijer A, Viti C, Marone C (2009) Fault zone fabric and fault weakness. Nature 462(7275):907-U98. https://doi.org/10.1038/nature08585

Dalaison M, Jolivet R, Rijsingen EM, Michel S (2022) The Interplay Between Seismic and Aseismic Slip Along the Chaman Fault Illuminated by InSAR. J Geophys Research-Solid Earth 126(12):e2021JB021935. https://doi.org/10.1029/2021JB021935

Devaraj S, Yarrakula K (2020) Assessment of topographical and atmospheric errors in Sentinel 1 derived DInSAR. Geocarto Int 37(8):2424–2440. https://doi.org/10.1080/10106049.2020.1822926

Fattahi H, Amelung F (2013) DEM Error Correction in InSAR time series. IEEE Trans Geosci Remote Sens 51(7):4249–4259. https://doi.org/10.1109/TGRS.2012.2227761

Friedrich AM, Wernicke BP, Niemi NA, Bennett RA, Davis JL (2003) Comparison of geodetic and geologic data from the Wasatch region, Utah, and implications for the spectral character of Earth deformation at periods of 10 to 10 million years. J Geophys Research-Solid Earth 108(B4):2199. https://doi.org/10.1029/2001JB000682

Geological diagram of V-type fault. https://www.facebook.com/engineeringinfinity.co/posts/a-spectacular-v-shaped-fault-at-zanjan-on-the-road-between-tabriz-and-tehran-in-/926316871506483. Accessed 10 May 2023.

Ha S, Son M, Seong YB (2022) active fault trace identification Using a LiDAR high-resolution DEM: a case study of the central Yangsan Fault. Korea Remote Sensing 14(19):4838. https://doi.org/10.3390/rs14194838

He JK, Vernant P, Chéry J, Wang WM, Lu SJ, Ku WF, Xia WH, Bilham R (2013) Nailing down the slip rate of the Altyn Tagh fault. Geophys Res Lett 40(20):5382–5386. https://doi.org/10.1002/2013GL057497

Henriquet M, Peyret M, Dominguez S, Barreca G, Monaco C, Mazzotti S (2022) Present-day surface deformation of sicily derived from Sentinel-1 InSAR time-series. J Geophys Research-Solid Earth 127(3):e2021JB023071. https://doi.org/10.1029/2021JB023071

Hong SY, Liu MA, Liu T, Dong YF, Chen LZ, Meng GJ, Xu YR (2022) Fault source model and stress changes of the 2021 Mw 7.4 Maduo earthquake, China, constrained by InSAR and GPS measurements. Bull Seismol Soc Am 112(3):1284–1296. https://doi.org/10.1785/0120210250

Huang X, Hong SY, Jin HL, Sun K, Jin Y (2021) Analysis of current deformation characteristics of the Jiali-Bengcuo fault. Proc Geophys 37(1):30–40. https://doi.org/10.6038/pg2022FF0103

Hussain E, Hooper A, Wright TJ, Walters RJ, Bekaert DPS (2016) Interseismic strain accumulation across the central North Anatolian Fault from iteratively unwrapped InSAR measurements. J Geophys Research-Solid Earth 121(12):9000–9019. https://doi.org/10.1002/2016JB013108

Kreemer C, Blewitt G, Klein EC (2014) A geodetic plate motion and global strain rate model. Geochem Geophys Geosyst 15(10):3849–3889. https://doi.org/10.1002/2014GC005407

Li YS, Tian YF, Yu C, Su Z, Jiang WL, Li ZH, Zhang JF, Luo Y, Li BQ (2020) Present-day interseismic deformation characteristics of the Beng Co-Dongqiao conjugate fault system in central Tibet: implications from InSAR observations. Geophys J Int 221(1):492–503. https://doi.org/10.1093/gji/ggaa014

Li HR, Bai L, Zhan HL (2021) Research progress of Jiali fault activity. Rev Geophys Planet Phys 52(2):182–193. https://doi.org/10.16738/j.dqyxx.2020-019

Liang MJ, Wu WW, Yang Y, Du F, Zhou WY, Zuo H, Liao C, Liu S, Zhang HP (2022) Late quaternary fault activity and deformation mechanism in the eastern Tibet Plateau (Dari fault, Bayan Har Block). Quatern Int 656:26–36. https://doi.org/10.1016/j.quaint.2022.09.009

Liu XH, Yao X, Yao JM (2022) Accelerated movements of Xiaomojiu landslide observed with SBAS-InSAR and three-dimensional measurements, upper Jinsha river, eastern Tibet. Appl Sciences-Basel 12(19):9758. https://doi.org/10.3390/app12199758

Lyons S, Sandwell D (2003) Fault creep along the southern San Andreas from interferometric synthetic aperture radar, permanent scatterers, and stacking. J Geophys Research-Solid Earth 108(B1):2047. https://doi.org/10.1029/2002JB001831

Mao WF, Wang XW, Liu GX, Ma PF, Zhang R, Ma ZF, Tang J, Lin H (2023) Ionospheric phase delay correction for time series multiple-aperture InSAR constrained by polynomial deformation model. IEEE Trans Geosci Remote Sens 20:4006605. https://doi.org/10.1109/LGRS.2023.3281343

Nissen E, Cambaz MD, Gaudreau É, Howell A, Karasözen E, Savidge E (2022) A reappraisal of active tectonics along the Fethiye-Burdur trend, Southwestern Turkey. Geophys J Int 230(2):1030–1051. https://doi.org/10.1093/gji/ggac096

Özbey V, Sengör AMC, Özeren MS (2022) Tectonics in a very slowly deforming region in an orogenic belt. Tectonophysics 827:229272. https://doi.org/10.1016/j.tecto.2022.229272

Qu Q, Daout S, Weiss JR, Shen L, Lazecky M, Wright TJ, Parsons BE (2022) Large-Scale Interseismic Strain Mapping of the NE Tibetan Plateau from Sentinel-1 Interferometry. J Geophys Research-Solid Earth 127(6):e2022JB024176. https://doi.org/10.1029/2022JB024176

Ren JW, Shen J, Cao ZQ, Wang YP (2000) Quaternary faulting of Jiali fault, southeast Tibetan plateau. Seismol Geol 22(4):344–350. https://doi.org/10.3969/j.issn.0253-4967.2000.04.002

Scott C, Bunds M, Shirzaei M, Toke N (2021) Creep along the Central San Andreas fault from surface fractures, topographic differencing, and InSAR. J Geophys Research-Solid Earth 125(10):e2020JB019762. https://doi.org/10.1029/2020JB019762

Shen J, Wang YP, Ren JW, Cao ZQ (2003) Quaternary dextral shearing and crustal movement in southeast Tibetan plateau. Xingjiang Geol 21(1):120–125. https://doi.org/10.3969/j.issn.1000-8845.2003.01.019

Song J, Tang FT, Deng JH, Cao ZQ, Zhou B, Xiao GR, Chen WT, Ge WP (2011) Study on current movement characteristics and numerical simulation of the main faults around Eastern Syntaxis. Chin J Geophys 54(6):1536–1548. https://doi.org/10.3969/j.issn.0001-5733.2011.06.013

Song J, Tang FT, Deng ZH, Xiao GR, Chen WT (2013) Late quaternary movement characteristic of Jiali Fault in Tibetan Plateau. Acta Scientiarum Naturalium Universitatis Pekinensis 49(6):973–980. https://doi.org/10.13209/j.0479-8023.2013.129

Tang FT, Song J, Cao ZQ, Deng ZH, Wang M, Xiao GR, Chen WT (2010) The movement characters of main faults around Eastern Himalayan Syntaxis revealed by the latest GPS data. Chin J Geophys 53(9):2119–2128. https://doi.org/10.3969/j.issn.0001-5733.2010.09.012

Wang M, Shen ZK (2020) Present-day crustal deformation of continental China derived from gps and its tectonic implications. J Geophys Research-Solid Earth 125(2):4. https://doi.org/10.1029/2019JB018774

Wang YZ, Wang EN, Shen ZK, Wang M, Gan WJ, Qiao XJ, Meng GJ, Li TM, Tao W, Yang YL (2008) GPS-constrained inversion of present-day slip rates along major faults of the Sichuan-Yunnan region, China. Sci China Series D-Earth Sci 51(9):1267–1283. https://doi.org/10.1007/s11430-008-0106-4

Wang ZX, Lawrence J, Ghail R, Mason P, Carpenter A, Agar S, Morgan T (2022) Characterizing micro-displacements on active faults in the Gobi desert with time-series InSAR. Applied Sciences-Basel 12(9):4222. https://doi.org/10.3390/app12094222

Wicks C, Weaver C, Bodin P, Sherrod B (2013) InSAR Evidence for an active shallow thrust fault beneath the city of Spokane Washington, USA. J Geophys Research-Solid Earth 118(3):1268–1276. https://doi.org/10.1002/jgrb.50118

Yao JM, Yao X, Wu ZQ, Liu XH (2020) Research on surface deformation of ordos coal mining area by integrating multitemporal D-InSAR and offset tracking technology. J Sens 2021:6660922. https://doi.org/10.1155/2021/6660922

Yao X, Chen YP, Liu DL, Zhou ZK, Liesenberg V, Marcato J, Li J (2021) Average-DInSAR method for unstable escarpments detection induced by underground coal mining. Int J Appl Earth Obs Geoinf 103:102489. https://doi.org/10.1016/j.jag.2021.102489

Yao JM, Lan HX, Li LP, Cao YM, Wu YM, Zhang YX, Zhou CD (2022a) Characteristics of a rapid landsliding area along Jinsha River revealed by multi-temporal remote sensing and its risks to Sichuan-Tibet railway. Landslides 19(3):703–718. https://doi.org/10.1007/s10346-021-01790-7

Yao JM, Yao X, Liu XH (2022b) Landslide Detection and Mapping Based on SBAS-InSAR and PS-InSAR: a case study in Gongjue County, Tibet. China Remote Sens 14(19):4728. https://doi.org/10.3390/rs14194728

Yao JM, Yao X, Zhao Z, Liu XH (2023) Performance comparison of Landslide susceptibility mapping under multiple machine-learning based models considering InSAR deformation: a case study of the upper Jinsha river. Geomat Nat Haz Risk 14(1):2212833. https://doi.org/10.1080/19475705.2023.2212833

Zhang Y, Liu CJ, Zhang WT, Jiang FY (2019) Present-day deformation of the Gyaring Co fault zone, central Qinghai-Tibet Plateau, determined using synthetic aperture radar interferometry. Remote Sens 11(9):1118. https://doi.org/10.3390/rs11091118

Zhang L, Liang SM, Yang XP, Gan WJ, Dai CL (2021) Geometric and kinematic evolution of the Jiali fault, eastern Himalayan Syntaxis. J Asian Earth Sci 212:104722. https://doi.org/10.1016/j.jseaes.2021.104722

Zhang BC, Zhu W, Ding XL, Wang CS, Wu SB, Zhang Q (2022a) A review of methods for mitigating ionospheric artifacts in differential SAR interferometry. Geodesy Geodyn 13(2):160–169. https://doi.org/10.1016/j.geog.2021.12.001

Zhang WT, Ji LY, Zhu LY, Liu CJ, Jiang FY, Xu XX (2022b) Current slip and strain rate distribution along the Ganzi-Yushu-Xianshuihe fault system based on InSAR and GPS observations. Front Earth Sci 10:821761. https://doi.org/10.3389/feart.2022.821761

Zhang YF, Gong WY, Shan XJ, Wang CS (2022c) Extension in the West Kunlun Mountains, NW Tibet: Insights from seismicity and analytical modeling. Tectonophysics 839:229526. https://doi.org/10.1016/j.tecto.2022.229526

Zhao B, Huang Y, Zhang CH, Wang W, Tan K, Du RL (2015) Crustal deformation on the Chinese mainland during 1998–2014 based on GPS data. Geodesy and Geodynamics 6(1):7–15. https://doi.org/10.1016/j.geog.2014.12.006

Zhao DZ, Qu CY, Shan XJ, Bürgman R, Gong WY, Zhang GH (2018) Spatiotemporal evolution of postseismic deformation following the 2001 Mw7.8 Kokoxili, China, earthquake from 7 Years of Insar observations. Remote Sens 10(12):1988. https://doi.org/10.3390/rs10121988

Zhao DZ, Qu CY, Bürgman R, Gong WY, Shan XJ, Qiao X, Zhao L, Chen H, Liu L (2022) Large-scale crustal deformation, slip-rate variation, and strain distribution along the Kunlun Fault (Tibet) from Sentinel-1 InSAR observations (2015–2020). J Geophy Research-Solid Earth 127(1):e2021JB022892. https://doi.org/10.1029/2021JB022892

Zhong N, Guo CB, Huang XL, Wu RA, Ding YY, Zhang XB, Li HB (2021) Late Quaternary activity and paleoseismic records of the middle south section of the Jiali-Chayu fault. Acta Geol Sin 95(12):3642–3659. https://doi.org/10.1976/j.cnki.dizhixuebao.2021069

Zhu LY, Ji LY, Jiang FY (2020) Variations in locking along the east Kunlun fault, Tibetan Plateau, China, using GPS and leveling data. Pure Appl Geophys 177(1):215–231. https://doi.org/10.1007/s00024-019-02231-2

Publisher's Note